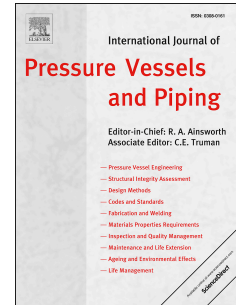# Accepted Manuscript

Application of failure assessment diagram methods to cracked straight pipes and elbows

R.A. Ainsworth, M. Gintalas, M.K. Sahu, J. Chattopadhyay, B.K. Dutta

Please cite this article as: Ainsworth RA, Gintalas M, Sahu MK, Chattopadhyay J, Dutta BK, Application of failure assessment diagram methods to cracked straight pipes and elbows, *International Journal of Pressure Vessels and Piping* (2016), doi: 10.1016/j.ijpvp.2016.10.005.

This is a PDF file of an unedited manuscript that has been accepted for publication. As a service to our customers we are providing this early version of the manuscript. The manuscript will undergo copyediting, typesetting, and review of the resulting proof before it is published in its final form. Please note that during the production process errors may be discovered which could affect the content, and all legal disclaimers that apply to the journal pertain.

Application of Failure Assessment Diagram Methods to Cracked Straight Pipes and Elbows

R A Ainsworth[1], M Gintalas[2], M K Sahu[3], J Chattopadhyay[3], B K Dutta[3]

1. The University of Manchester, Pariser Building, Sackville Street, Manchester M13 9PL, UK.
2. The University of Manchester, Pariser Building, Sackville Street, Manchester M13 9PL, UK; corresponding author, email address: marius.gintalas@manchester.ac.uk, telephone: +447551719130.
3. Reactor Safety Division, Hall-7, Bhabha Atomic Research Centre, Mumbai 400085, India.

Abstract

This paper reports fracture assessments of large-scale straight pipes and elbows of various pipe diameters and crack sizes. The assessments estimate the load for ductile fracture initiation using the failure assessment diagram method. Recent solutions in the literature for stress intensity factor and limit load provide the analysis inputs. An assessment of constraint effects is also performed using recent solutions for elastic T-stress. It is found that predictions of initiation load are close to the experimental values for straight pipes under pure bending. For elbows, there is generally increased conservatism in the sense that the experimental loads are greater than those predicted. The effects of constraint are found not to be a major contributor to the initiation fracture assessments but may have some influence on the ductile crack extension.

Keywords: Pipe, elbow, crack, failure assessment diagram, fracture

1 Introduction

In a wide range of industries, the structural integrity assessment of piping components containing defects is required to demonstrate safe and reliable operation. For example, leak-before-break (LBB) assessments of primary piping systems of some nuclear power plant assume the presence of cracks and demonstrate that such cracks lead to detectable leakage before pipe burst. There have been many studies addressing the defect tolerance of piping components, some addressing the influence of defects on the collapse load, others addressing fracture using linear and non-linear fracture mechanics. This has led to the inclusion of procedures for assessment of piping components within more general fracture assessment approaches such as R6 [1], BS7910 [2], API 579 [3], RSE-M [4] and others.

Large-scale experimental validation of the methods for assessment of piping components is available. For example, recently Zhu and Leis [5] examined the burst pressure prediction of over 100 uncracked pipes while Bedairi et al. [6] examined the influence of corrosion defects on fracture. Another study involved a large number of large-scale tests on straight pipes and elbows of various pipe sizes and crack configurations subjected to different loading conditions, as summarised by Chattopadhyay et al. [7, 8] and assessed recently in [9].

Although analyses of pipes and elbows have been available for some years, the major closed form inputs into fitness-for-service assessments, such as limit load and stress intensity factor solutions for pipes and elbows, are still being improved. The limit load solution for defective pipes, despite decades of research, are still being refined. For example, solutions have recently been developed for thick-walled cylinders with circumferential surface defects under any combination of axial force, global bending moment and internal pressure [10, 11].

The pipe geometry is relatively simple and can be solved semi-analytically. However, the elbow geometry brings additional challenges. For instance, there is a lack of accurate solutions for elastic stress distributions in defect-free elbows loaded by internal pressure or in-plane bending moment and research is being continued in this area [12, 13]. Usually the elbow cross-section is considered to be circular with uniform wall thickness. In practice, according to [14, 15, 16, 17] the elbow cross-section

has shape imperfections, which come from manufacturing process. The shape deviation influences both elastic solutions and the collapse load. However, recently it has been shown that for some cracked pipe bends, an estimate of J for non-uniform section thickness can be made using the average thickness [18]. Therefore, the geometry of the components analysed in this study has been considered with no geometrical deviations.

Limit load solutions in this paper are based on an elastic-perfectly plastic material assumption. Limit loads for component may be obtained from an equilibrium stress distribution which satisfies the chosen yield criterion. Various yield criteria, such as Tresca, von Mises and twin shear stress can be employed. Attempts to include material hardening properties into limit load solutions have also started to appear in the literature [19]. However, the influence of chosen yield criterion is more significant then strain hardening exponent. Therefore, as can be seen from the review [20], the limit load solution is presented as a function of component and crack geometry only.

This paper revisits the experimental data on large-scale piping components of Chattopadhyay et al. [7, 8]. Although these data have been assessed using a number of fracture mechanics approaches as discussed in [9], recently there have been developments in both stress intensity factor, T-stress and limit load solutions for defective straight pipes and elbows [21-27]. This paper therefore uses these up-to-date solutions in conjunction with selected data from [7, 8] to examine the accuracy of codified fracture assessment procedures. First, Section 2 briefly summarises the experimental data, both from large-scale tests and related small-scale materials tests. Then, Section 3 presents the analytical inputs to be used in the fracture assessments of Section 4. Section 5 discusses the results before conclusions of the study are given in Section 6.

2 Summary of Experimental Data

2.1 Materials data from small-scale tests

Materials data have been obtained from standard tensile tests and compact tension (CT) and three-point bend (TPB) specimens for the SA 333 Grade 6 carbon steel used in the pipe and elbow tests. Results are presented in Table 1; the tensile and fracture toughness data depend on the diameter of the pipe used. Initiation fracture toughness values were obtained using stretch zone width (SZW) measurements at a crack growth of Δa=0.2mm. For the larger diameter pipes, fracture toughness data, as measured on both CT and TPB specimens, showed some variability as indicated in Table 1. The lower values in bold in the table are used for the baseline fracture assessments of the large-scale component tests which are described next.

Table 1. Properies of SA 333 Grade 6 steel as a function of pipe diameter

Outer diameter D_0, mm	219	406	460	610
Young's modulus, E, GPa	203	203	203	203
Poisson's ratio, ν	0.3	0.3	0.3	0.3
Yield stress, σ_y, MPa	288	312	302	323
Ultimate tensile stress, σ_u, MPa	420	459	517	496
Initiation fracture toughness, $J_{0.2}$, N/mm (measured at a SZW of 0.2mm)	220 (TPB a/W=0.51)	236 (TPB a/W=0.2)	**253 (CT a/W=0.45)** 349 (TPB a/W=0.54)	**228 (TPB a/W=0.26)** 375 (CT a/W=0.56) 351 (TPB a/W=0.62)

2.2 Large-scale component test data

2.2.1 Circumferentially through-wall cracked pipes

Fracture tests were carried out on cracked pipes and elbows under quasi-static monotonic loading. In total 45 tests consisting of 27 pipes of various sizes (200–400mm diameter) with surface and through-wall circumferential cracks of various angles (30–150°), and 18 elbows of various sizes (200–400 mm pipe diameter) with through-wall cracks of various angles (60–120°), locations (extrados/intrados/crown) and configurations (circumferential/axial) were loaded under in-plane bending. Additional tests also addressed combined bending and pressure. Of these tests, results for eight straight pipes and 13 elbows are used here for validation of the newly developed equations in [21-25]. More details of the tests are described in [7, 8].

Six pipes of SA333 Grade 6 steel were tested under static four-point bending as shown schematically in Figure 1. These 6 pipes denoted as SPBMTWC (Table 2) were fatigue pre-cracked. Two tests denoted as PRSPTWC8 (Table 2) were conducted under combined four-point bending and internal pressure, with the pressure applied first and then cracks sealed to ensure the pressure was maintained as the bending load was increased. These two pipes were not fatigue pre-cracked and had V-shape notches. Values of the total load applied to the pipes, the load-line displacement and crack length/growth were recorded during each test. The experimental load-displacement curves are shown in Figure 2. On each curve, the point of crack initiation is identified as the load at a ductile crack growth of 0.2mm, consistent with the fracture toughness data listed in Table 1.
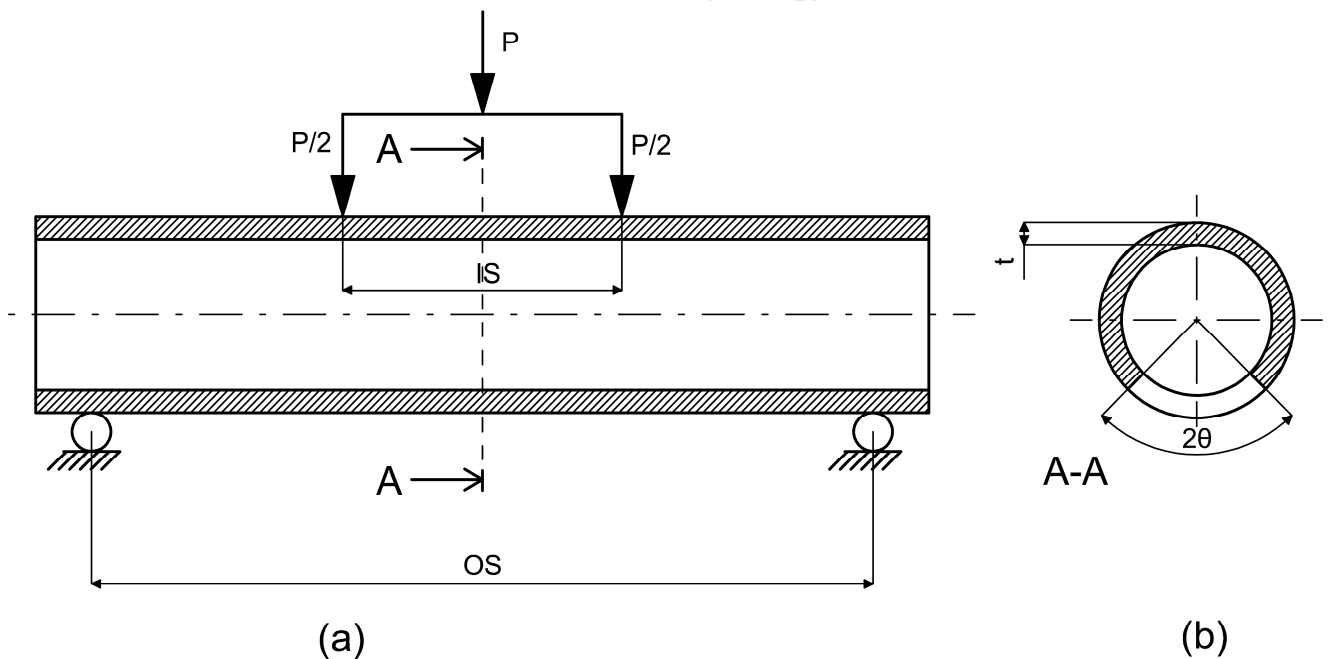

Fig. 1 (a) Loading configuration for the pipe tests, where Outer Span (OS) is distance between the supports and Inner Span (IS) is distance between the loading points; (b) Cross sectional view of a pipe with a through-wall crack

The geometries of the cracked pipes in terms of the outer diameter, D_0, thickness, t, mean radius, R_m, and total crack angle of the circumferential cracks, 2θ, are given in Table 2. Measurements of the inner (IS) and outer span (OS) dimensions and the experimental initiation loads, $P_{0.2}^{ex}$, determined at a crack extension of 0.2mm as shown in Figure 2, are also presented in Table 2.
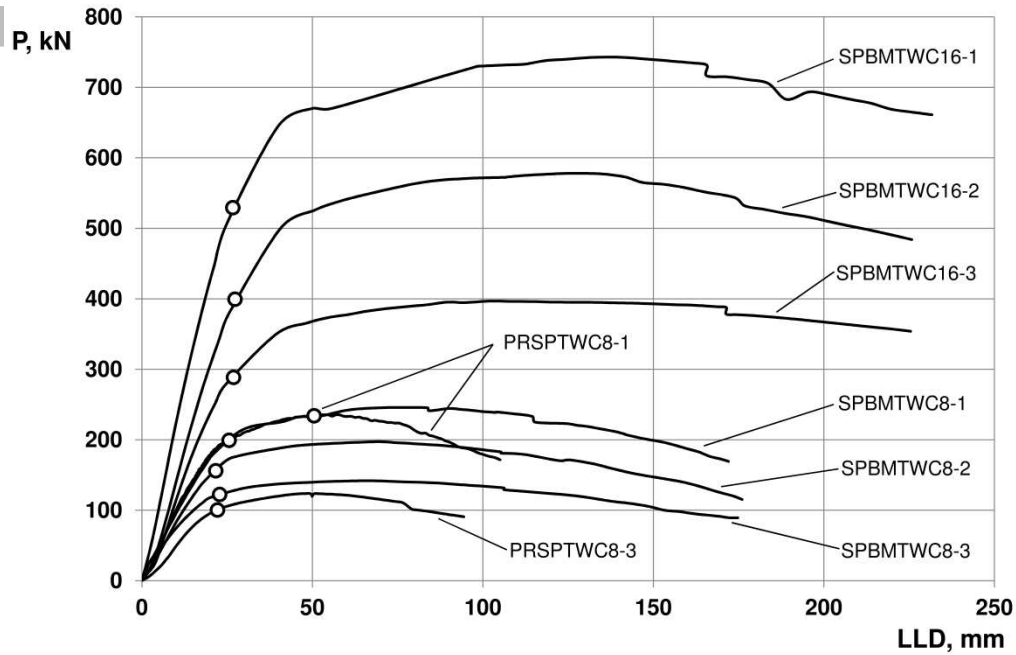
Fig. 2 Experimental load-line displacement (LLD) curves versus applied load, P, for each of the straight pipe tests, including the identified crack initiation points

Table 2. Dimensions of large-scale pipe tests and experimental values of initiation load at crack growth of 0.2mm

Test Number	Loading type	Outer Diameter D_0, mm	Thickness t, mm	$\dfrac{R_m}{t}$	Outer Span OS, mm	Inner Span IS, mm	Total crack angle 2θ	$\dfrac{\theta}{\pi}$	Experimental initiation load $P_{0.2}^{ex}$, kN (Δa =0.2mm)
SPBMTWC8-1	Four-Point Bend	219	15.15	6.73	4000	1480	65.6°	0.18	199.1
SPBMTWC8-2		219	15.10	6.75	4000	1480	93.9°	0.26	155.9
SPBMTWC8-3		219	15.29	6.66	4000	1480	126.4°	0.35	122.2
SPBMTWC16-1		406	32.38	5.77	5820	1480	96.0°	0.27	529.2
SPBMTWC16-2		406	32.15	5.81	5820	1480	126.3°	0.35	399.3
SPBMTWC16-3		406	32.36	5.77	5820	1480	157.8°	0.44	288.4
PRSPTWC8-1	Four-Point Bend	219	18.2	5.52	3374	990	90.52°	0.25	240.8
PRSPTWC8-3	Four-Point Bend + internal pressure	219	18.5	5.42	3480	990	152.8°	0.42	100.3

2.2.2 Circumferentially through-wall cracked elbows

Thirteen 90 degree elbows of SA333 Grade 6 steel with circumferential through-wall cracks, either at the intrados or extrados, were tested by applying static in-plane bending moment. The elbows which were cracked at the extrados were tested under closing mode and those cracked at the intrados were tested under opening mode. Straight pipes were welded to each side of an elbow and to flanges, bolted to circular plates, for connection to the loading. Fig. 3 is a schematic of an elbow test set up.
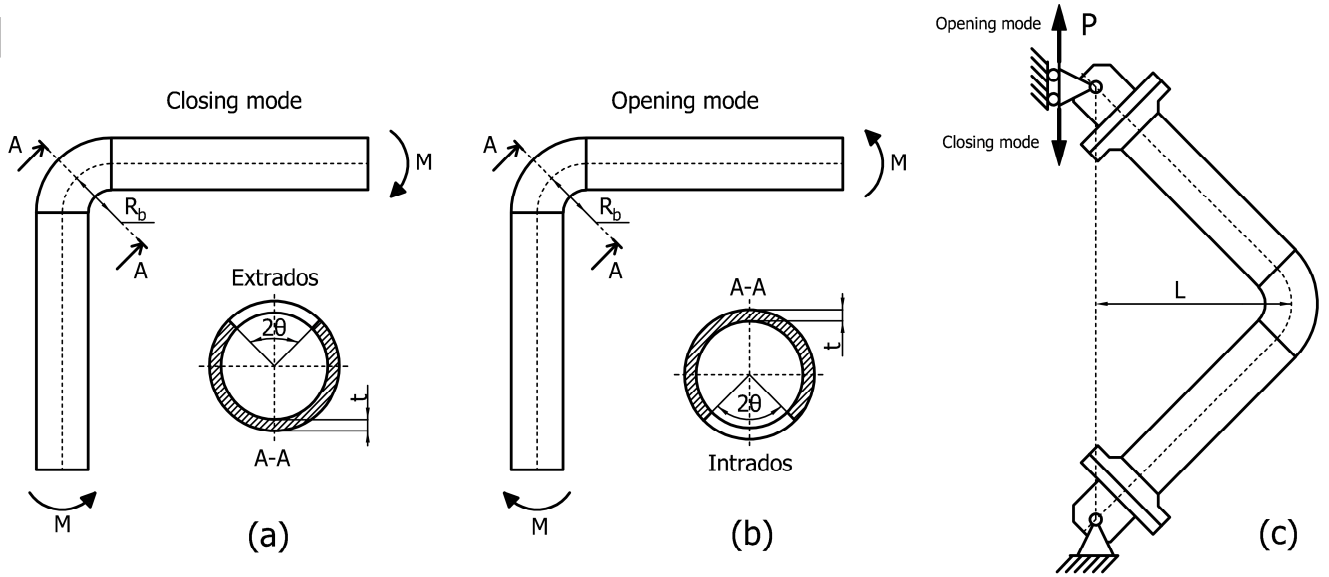
Fig. 3 Loading configuration of an elbow, under in plane bending moment: a) crack at extrados – closing mode, b) crack at intrados – opening mode; c) test set up

Table 3. Dimensions of elbows and experimental values of initiation load at crack growth of 0.2mm

Test Number	Outer Diameter D_0, mm	Thickness t, mm	$\dfrac{R_m}{t}$	λ	Bend Radius R_b, mm	Moment Arm length L, mm	Total crack angle 2θ	$\dfrac{\theta}{\pi}$	Experimental initiation load $P_{0.2}^{ex}$, kN $\Delta a = 0.2$mm
ELTWIN8-1	219	19.1	5.23	0.40	207	825.72	94.96°	0.26	113.0
ELTWIN8-2	219	18.8	5.32	0.39	207	825.72	125.16°	0.35	89.7
ELTWIN16-1	406	36.43	5.07	0.65	609	840.22	95.89°	0.27	647.6
ELTWIN16-2	406	36.85	5.01	0.66	609	840.22	122.79°	0.34	594.3
ELTWCIN18-2	460	52.2	3.91	0.86	685.5	1240	119.6°	0.33	1117.6
ELTWCIN18-1	460	51.1	4.00	0.84	685.5	1210	151.9°	0.42	668.0
ELTWCIN24-3	610	39.7	7.18	0.45	915	1150	118.3°	0.33	1321.3
ELTWEX8-4	219	19.3	5.17	0.40	207	825.72	98.24°	0.27	125.0
ELTWEX16-3	406	35.06	5.29	0.62	609	840.22	64.85°	0.18	1382.1
ELTWEX16-4	406	35.7	5.19	0.63	609	840.22	94.11°	0.26	1004.2
ELTWEX16-5	406	37.6	4.90	0.67	609	840.22	124°	0.34	748.4
ELTWCEXC24-2	610	39.9	7.14	0.45	915	1120	119.3°	0.33	1824.7
ELTWCEXC24-1	610	40.6	7.01	0.46	915	1120	148.4°	0.41	1411.2

The geometric properties of the elbows are given in Table 3 and are similar to those of the straight pipes but additionally include the bend radius, R_b and the elbow factor, λ, defined by

$$\lambda = tR_b / R_m^2 \tag{1}$$

Where the test number contains "IN", the elbows were cracked at the intrados and elbows cracked at the extrados have test numbers which contain "EX". It is important to note that the 18 and 24 inch elbows from Table 3 were not fatigue pre-cracked and had V-shape notches. The experimental loading arrangement is given in terms of the moment arm length, L, shown in Figure 3. Values of crack

initiation load for the thirteen elbow tests are listed in Table 3 and are identified on the load-displacement curves shown in Figures 4 and 5 for opening and closing bending modes, respectively.
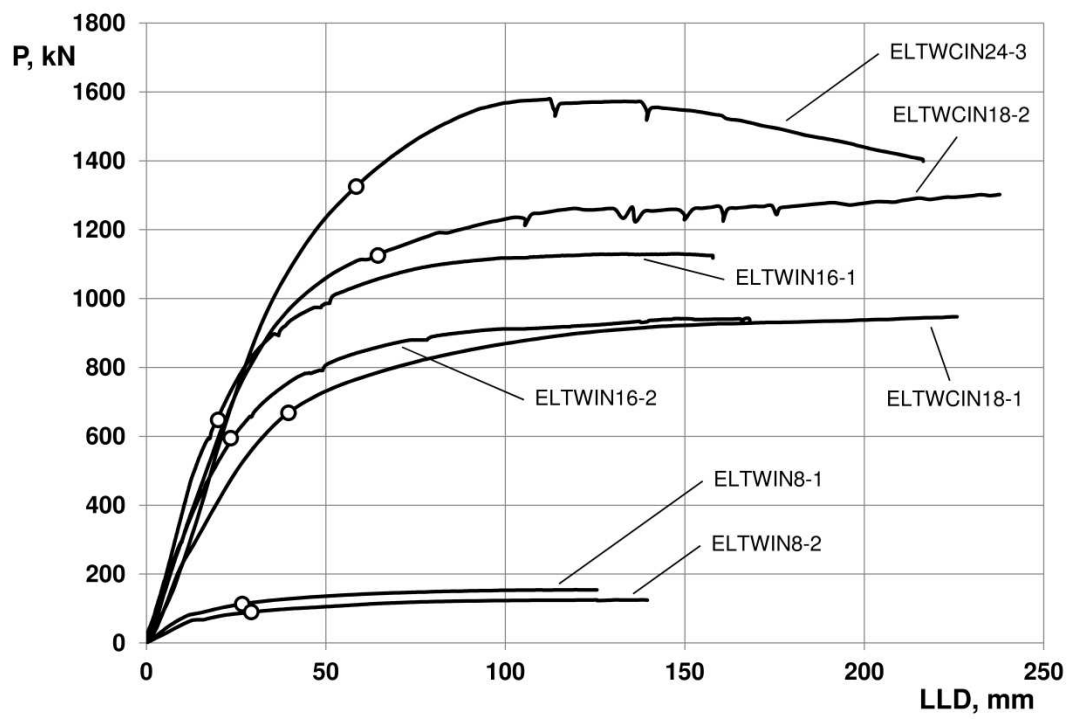

Fig. 4 Experimental load-line displacement (LLD) curves versus applied load, P, for each of the elbow tests under opening mode, including the identified crack initiation points
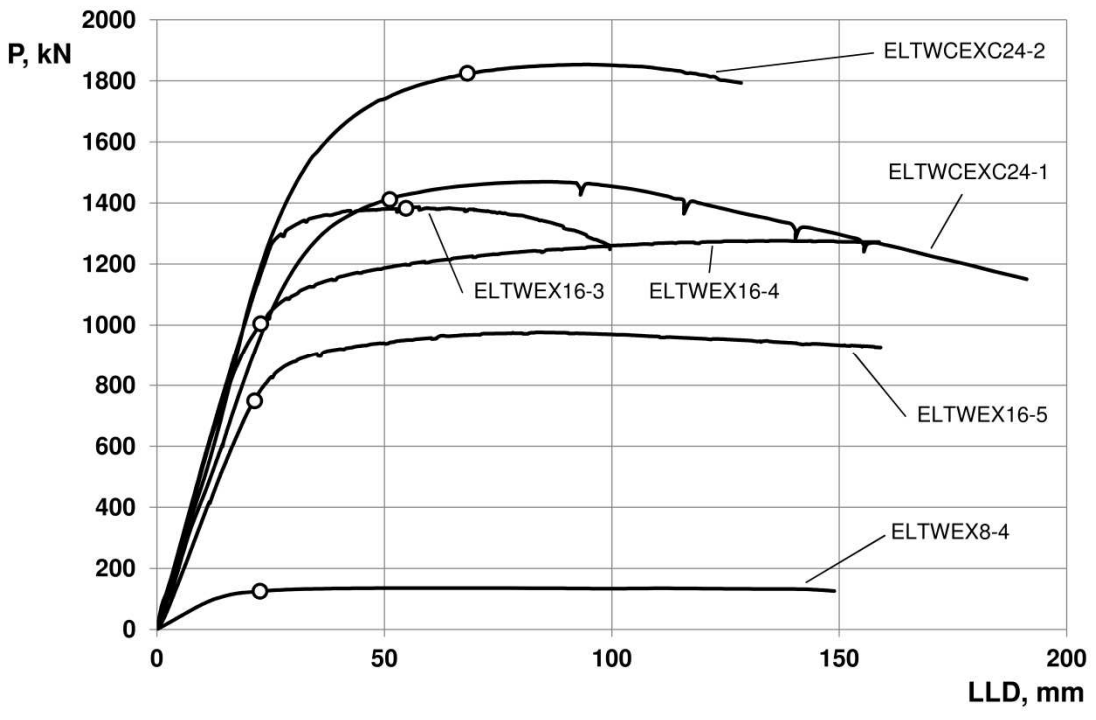

Fig.5 Experimental load-line displacement (LLD) curves versus applied load, P, for each of the elbow tests under closing mode, including the identified crack initiation points

3 Analytical Solutions for Input to the Fracture Assessments

3.1 Stress Intensity Factor Solutions

3.1.1 Stress intensity factor solutions for circumferentially through-wall cracked pipes under in-plane bending moment and internal pressure

In order to apply failure assessment diagram methods to the cracked pipes, it is necessary to evaluate the stress intensity factor, K_I. The following solution for bending moment [1, 28] was used:

$$K_{Ib} = F_b \sigma_b \sqrt{\pi a} \tag{2}$$

where the bending stress, σ_b, is defined in terms of the bending moment M_b as

$$\sigma_b = M_b / \left[\pi R_m^2 t \right] \tag{3}$$

The correction function, F_b, in equation (2) is

$$F_b = 1 + A \left[4.5967 \left(\frac{\theta}{\pi} \right)^{1.5} + 2.6422 \left(\frac{\theta}{\pi} \right)^{4.24} \right] \quad \text{for} \quad 0 < \frac{\theta}{\pi} \leq 0.55 \tag{4}$$

where

$$A = \left[0.125 (R_m / t) - 0.25 \right]^{0.25} \quad \text{for} \quad 5 \leq R_m / t \leq 10 \tag{5}$$

The stress intensity factor solution for internal pressure is given in terms of the corresponding axial stress

$$\sigma_t = \frac{(R_m - t/2)^2}{2 R_m t} p \tag{6}$$

as [1, 15]:

$$K_{It} = F_t \sigma_t \sqrt{\pi a} \tag{7}$$

where the correction function, F_t, in equation (7) is

$$F_t = 1 + A \left[5.3303 \left(\frac{\theta}{\pi} \right)^{1.5} + 18.773 \left(\frac{\theta}{\pi} \right)^{4.24} \right] \quad \text{for} \quad 0 < \frac{\theta}{\pi} \leq 0.55 \tag{8}$$

where A is again given by equation (5).

For each pipe the values of the ratios R_m / t and θ / π are included in Table 2. All the pipes tested are within the validity limits on R_m / t and θ / π in eqns (4, 5, 8).

3.1.2 Stress intensity factor solutions for circumferentially through-wall cracked elbows under in-plane bending moment

In order to calculate the stress intensity factor for elbows, the solution recently developed in [21] has been used:

$$K_{Ib} = F_b \sigma_b \sqrt{\pi a} \qquad (9)$$

where the bending stress, σ_b, is again given by equation (3). Values for the correction function F_b are presented in tabular form in [21] for particular elbow sizes as functions of R_m/t, R_b/R_m and θ/π. The solutions for F_b which cover the range of elbows tested are presented in Tables 4 and 5, as functions of the ratios R_m/t, θ/π and R_b/R_m, the first two of which are included in Table 3 for each elbow, and $R_b/R_m = \lambda R_m/t$ can be deduced from Table 3. Values are only given for solutions where the crack fully opens (see [21]). The values of R_m/t, θ/π and R_b/R_m in Tables 4 and 5 cover the full range of elbows tested.

Table 4. Values of the function F_b for a crack at the centre of the elbow extrados - closing mode

R_m/t	R_b/R_m	θ/π			
		0.1	0.2	0.3	0.5
3	2	0.609	0.856	1.189	2.176
	3	0.751	0.978	1.280	2.219
	4	0.846	1.057	1.336	2.239
5	2	0.374	0.722	1.231	2.601
	3	0.570	0.901	1.347	2.541
	4	0.727	1.036	1.429	2.512
10	2	-	-	1.119	3.509
	3	-	0.505	1.322	3.287
	4	0.273	0.749	1.481	3.131

Table 5. Values of the function F_b for a crack at the centre of the elbow intrados - opening mode

R_m/t	R_b/R_m	θ/π			
		0.1	0.2	0.3	0.5
3	2	1.037	1.335	1.706	2.726
	3	1.072	1.305	1.616	2.593
	4	1.076	1.275	1.558	2.517
5	2	0.765	1.257	1.884	3.313
	3	0.892	1.288	1.783	3.068
	4	0.964	1.281	1.703	2.918
10	2	-	0.792	2.02	4.625
	3	0.359	0.993	1.996	4.193
	4	0.510	1.099	1.930	3.896

3.2 Limit Load Solutions

3.2.1 Limit load solutions for circumferentially through-wall cracked pipes under combined four-point bending and internal pressure

For combined bending moment and internal pressure, a limit load is given by Lei et al [24] and the limit moment, M_L, depends on the limit pressure, p_L, according to the following:

$$M_L = 2R_m^2 t\sigma_y \left[(A_1 - A_2)\sin\beta - A_1\sin\theta\right]\left[1 + (1/12)(t/R_m)^2\right]\left[1 - (1/12)(t/R_m)\right]^{-2} \tag{10}$$

where

$$\beta = \frac{\pi A_1}{A_1 - A_2}\left[1 - \frac{\theta}{\pi} - \frac{n_p\left[1 - (1/12)(t/R_m)\right]^2}{A_1}\right]$$

$$n_p = \frac{p_L R_m}{2t\sigma_y}\left[1 - (1/12)(t/R_m)\right]^2 \tag{11}$$

$$A_1 = \left[1 - (t/R_m)\right]n_p + \sqrt{\left[1 - (1/12)(t/R_m)\right]^4 - 3n_p^2}$$

$$A_1 = \left[1 - (t/R_m)\right]n_p - \sqrt{\left[1 - (1/12)(t/R_m)\right]^4 - 3n_p^2}$$

where the solution must satisfy $\beta + \theta \leq \pi$ (which it does for the cases examined here) and the ratio of the limit moment and limit pressure must equal the ratio of applied moment and pressure, i.e.

$$M/M_L = p/p_L \tag{12}$$

Note that although the pipes were loaded under constant pressure followed by increasing bending moment, the value of the limit load parameter, L_r of eqn (13) below, corresponding to the experimental load at crack initiation, is evaluated from values of bending moment and pressure which satisfy eqn (12) so that

$$L_r = M/M_L = p/p_L \tag{13}$$

This can require iteration to solve eqns (10) and (11). Similarly, the evaluation of predicted initiation moment can require iteration so that equation (13) is satisfied with p=10MPa. For the majority of cases in Table 2 where p=0, the solution simplifies to

$$M_L = 4R_m^2 t\sigma_y \left[\cos(\theta/2) - (1/2)\sin\theta\right]\left[1 + (1/12)(t/R_m)^2\right] \tag{14}$$

3.2.2 Limit load solutions for circumferentially through-wall cracked elbows under in-plane bending

3.2.2.1 Closing mode

The limit moment for a defective pipe bend is taken as the product of the limit moment for an un-cracked elbow M_{Lu} and a weakening factor X:

$$M_L = M_{Lu}X \tag{15}$$

The solution for a defect free elbow under closing moment was recently developed in [22]:

$$\frac{M_{Lu}}{M_L^p} = \begin{cases} \left(1 + \dfrac{0.22}{\lambda^{1.028+0.12(R_b/R_m)}}\right)^{-1} & \text{for} \quad \lambda \leq 1 \\[3mm] \left(1 + \dfrac{0.22}{\lambda^{1.313}}\right)^{-1} & \text{for} \quad \lambda > 1 \end{cases} \tag{16}$$

where M_L^p is the limit moment for the uncracked straight pipe:

$$M_L^p = 4R_m^2 t\sigma_y \tag{17}$$

and λ is the elbow factor defined in eqn (1).

The weakening factor due to the presence of the crack is [23]:

$$X = \begin{cases} 1.0 & \text{for} \quad 0 \leq \theta/\pi < 0.21 \\ 1.44 - 2.1(\theta/\pi) & \text{for} \quad 0.21 \leq \theta/\pi < 0.5 \\ 3.12(1-\theta/\pi)^3 & \text{for} \quad 0.5 \leq \theta/\pi \leq 1.0 \end{cases} \tag{18}$$

The values of the ratio θ/π and λ are included in Table 3 for each elbow tested.

3.2.2.2 Opening mode

The limit moment solution for a defective pipe bend is again taken as the product of the solution for an un-cracked elbow M_{Lu} and a weakening factor X as in eqn (15). The solution for a defect free elbow under opening moment was again recently developed in [22] as:

$$M_{Lu}/M_L^p = 0.8908 + 0.2502\ln(\lambda) \qquad \text{for} \qquad 0.1 \leq \lambda \leq 1.0 \tag{19}$$

where the uncracked straight pipe limit moment is again given by eqn (17). The weakening factor due to the presence of the crack in this case is [29]:

$$X = 1.127 - 1.8108(\theta/\pi) \qquad \text{for} \quad 0.125 \leq \theta/\pi < 0.41 \tag{20}$$

3.3 Constraint parameter solutions for straight pipes

In order to assess whether loss of constraint is relevant to the pipe fracture assessments, values of the elastic T-stress were calculated following the solutions presented in [25]. There normalised T-stress solutions are given in the form:

$$T/\sigma = C_1 + C_2(\theta/\pi)^2 + C_3(\theta/\pi)^4 + C_4(\theta/\pi)^6 + C_5(\theta/\pi)^8 + C_6(\theta/\pi)^{10} \tag{21}$$

where the solutions are normalised by $\sigma = M/(\pi R_m^2 t)$ in bending and for pressure by $\sigma = P_a/(2\pi R_m t)$ where P_a is the end load due to the pressure. The coefficients C_i $(i = 1-6)$ in eqn (21) are functions of the radius to thickness ratio R_m/t:

$$C_i = C_{i0} + C_{i1}(R_m/t) + C_{i2}((R_m/t)^2 \tag{22}$$

where the coefficients C_{ij} are given in Table 6.

Table 6. Constraint coefficients in eqns (21) and (22)

i		Constraint Coefficient		
		C_{i0}	C_{i1}	C_{i2}
tension	1	-0.9613	-0.0062	0.0003
	2	1.0457	0.8247	-0.0278
	3	33.671	-22.126	0.5365
	4	-210.6	120.23	-1.5892
	5	852.45	-322.72	0.2417
	6	-1272	351.17	3.9989
bending	1	-0.934	-0.01	0.0005
	2	4.3575	1.2671	-0.0451
	3	74.273	-35.312	0.9889
	4	-680.39	266.98	-6.3389
	5	2688.6	-957.82	20.135
	6	-3852.8	1325	-25.744

4. Defect Assessment

4.1 R6 Option 1 defect assessment procedure

The failure assessment diagram (FAD) approach is used in R6 [1] and also in a number of other codes [2-3]. The FAD uses the parameters L_r and K_r, which are defined for ductile initiation assessments by

$$L_r = M_b / M_L(a_0, \sigma_y) \tag{23}$$

and

$$K_r = K_I / K_{mat}(a_0) \tag{24}$$

where a_0 is the initial crack size and $K_{mat}(a_0)$ is the initiation fracture toughness. The initiation fracture toughness in the form of J-integral at 0.2mm crack growth, $J_{0.2}$, can be found in Table 1. The experimental initiation load is presented in Tables 2 and 7 for pipes and in Table 8 for elbows. For combined pressure and bending, K_I is the total stress intensity factor for the combined loading and L_r may be defined from eqn (23) or from the pressure ratio as in eqn (13). The limit load, M_L, for pipes is calculated using eqn (10) and for elbows using eqn (15). The stress intensity factor, K_I, for pipes is calculated from eqns (2) and (7) and for elbows from eqn (9). The bending moment, M_b, for pipes and elbows is defined from the applied load: for pipes $M_b = P(OS - IS)/2$ (see Table 2 and Fig.1), for elbows $M_b = L \cdot P$ (see Table 3 and Fig. 3 for L). Crack initiation is conceded when the values of K_r and L_r lie on the R6 Option 1 failure assessment curve

$$K_r = (1 + 0.5L_r^2)^{-0.5}[0.3 + 0.7\exp(-0.6L_r^6)] \tag{25}$$

or reach the cut-off

$$L_r = L_r^{max} = (\sigma_y + \sigma_u)/2\sigma_y \tag{26}$$

Material yield and ultimate stress values can be found from Table 1.

4.2 Defect assessment results for straight pipes

For the 6 straight pipes under pure bending, the predicted initiation loads are compared with the experimental initiation loads in Table 7. Also included in the table are the values of L_r and K_r at the predicted initiation loads. Figure 6 shows the assessment points (L_r, K_r) evaluated at the experimental initiation loads and the predicted initiation loads, plotted on the FAD. Of course, the assessment points for the predicted loads lie on the failure assessment curve. It can be seen that the predicted initiation loads are close to the experimental loads, with the percentage differences given in Table 7, and that ductile initiation occurs before plastic collapse.

Table 7 also includes the predicted initiation loads for the two pipes tested under combined pressure and bending, with again assessment points (L_r, K_r) evaluated at the experimental and predicted initiation loads, plotted on the FAD of Figure 6. As noted, in Section 3.2.1, some iteration is needed to evaluate L_r for the applied ratio of pressure and bending. It can be seen from Table 7 that the experimental initiation loads exceed the predicted values by about 30% and that ductile initiation occurs close to plastic collapse. This is discussed further in Section 6, as are the normalised T-stress solutions which are given in Table 7.

Table 7. Comparison of experimental and predicted initiation loads for pipes

Test Number	Experimental Initiation Load $P_{0.2}^{ex}$, kN		Predicted Initiation Load $P_{0.2}^{p}$, kN		Difference, % $\frac{(P_{0.2}^{p} - P_{0.2}^{ex})}{P_{0.2}^{ex}}100$	Normalised T-stress at $P_{0.2}^{ex}$, T/σ_y
	L_r	K_r	L_r	K_r		
SPBMTWC8-1	199.1		186.6		-6.3	-0.72
	1.0027	0.6779	0.9399	0.6353		
SPBMTWC8-2	155.9		142.6		-8.6	-0.58
	0.9830	0.7483	0.8986	0.6840		
SPBMTWC8-3	122.2		104.7		-14.3	-0.43
	1.0374	0.8106	0.8891	0.6946		
SPBMTWC16-1	529.2		539.9		2.0	-0.56
	0.7483	0.7951	0.7634	0.8110		
SPBMTWC16-2	399.3		397.2		-0.5	-0.39
	0.7586	0.8220	0.7546	0.8175		
SPBMTWC16-3	288.4		289.6		0.4	-0.17
	0.7857	0.7874	0.7892	0.7907		
PRSPTWC8-1	240.8		173.6		-27.9	-0.65
	1.2741	0.871	0.9458	0.6281		
PRSPTWC8-3	100.3		79.1		-21.2	-0.25
	1.2167	0.6846	1.0144	0.5397		

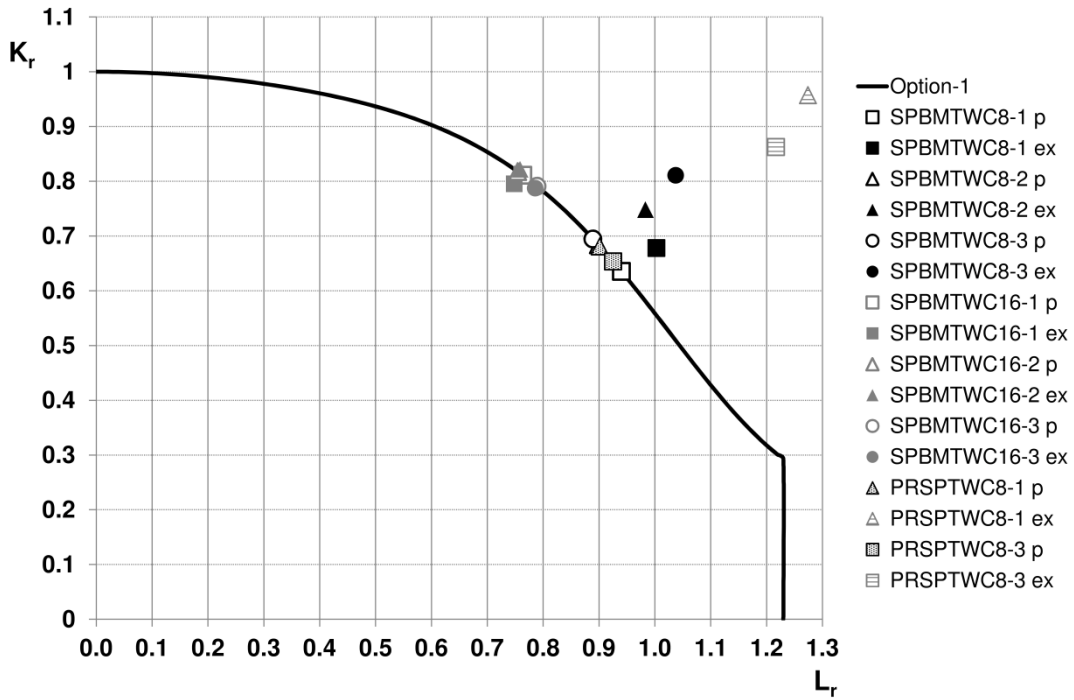**Fig. 6** Circumferentially through-wall cracked pipes. Predicted and experimental initiation load points (Δa=0.2 mm) on FAD

For the 6 through-wall cracked pipes under pure bending, initiation occurred before maximum load, as shown in Figure 2, and measurements of ductile crack extension as a function of load beyond initiation are available. These experimental crack growth versus load data have been converted to J-Δa tearing resistance curves by assuming that the experimental points lie on the Option 1 R6 curve, similar to the points on the FAD in Figure 6. However, in this case, this leads not to predicted loads but to predicted material J values. These predicted J values are plotted versus the experimental crack growth measurements in Fig. 7, where triangles represent the three 406 mm diameter pipes and circles represent the three 209 mm diameter pipes. It can be seen that that the circles and triangles form two separate areas, as illustrated by the dotted lines which bound the respective data. These results are discussed in Section 6.
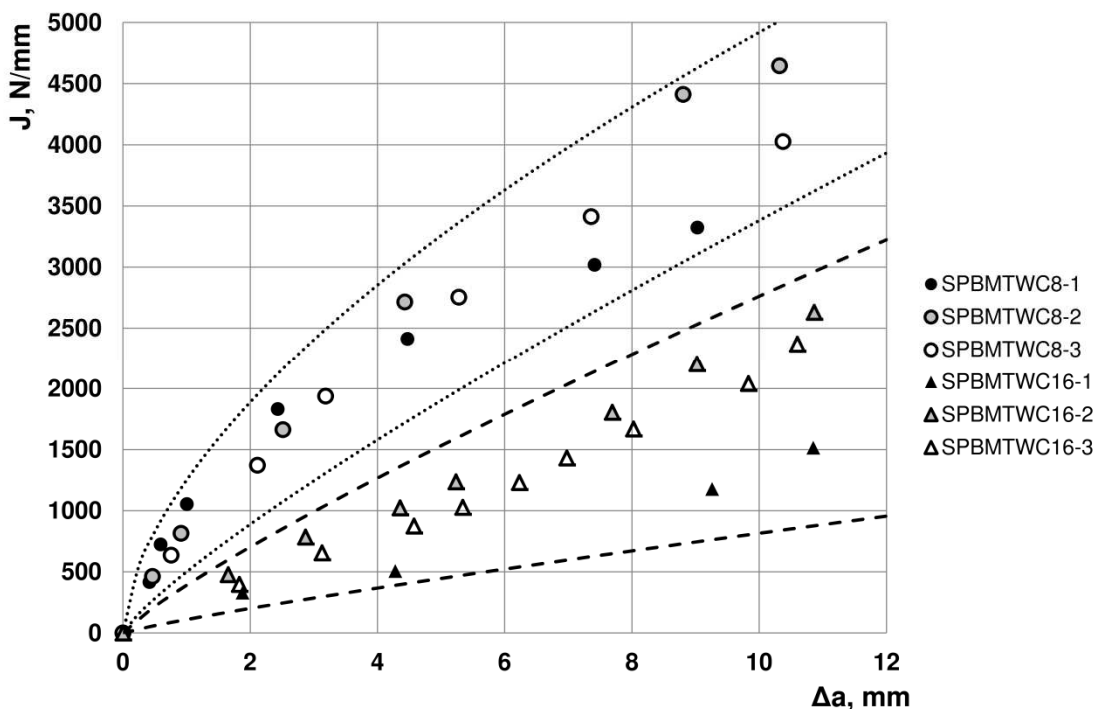

Fig. 7 Predicted J-Δa resistance curves for the straight pipes under pure bending

4.3. Defect assessment results for elbows

For the 13 elbows under opening and closing bending, the predicted ductile initiation loads are compared with the experimental initiation loads in Table 8. Also included in the table are the values of L_r and K_r at the predicted initiation loads. Figures 8 and 9 show the assessment points (L_r, K_r) evaluated at the experimental and predicted initiation loads, plotted on the FAD. It can be seen that the predicted initiation loads generally exceed the experimental loads, with the percentage differences given in Table 7, and that ductile initiation occurs before plastic collapse, although often close to $L_r = 1$. The results are discussed further in Section 6.

Table 8. Comparison of experimental and predicted initiation loads for elbows

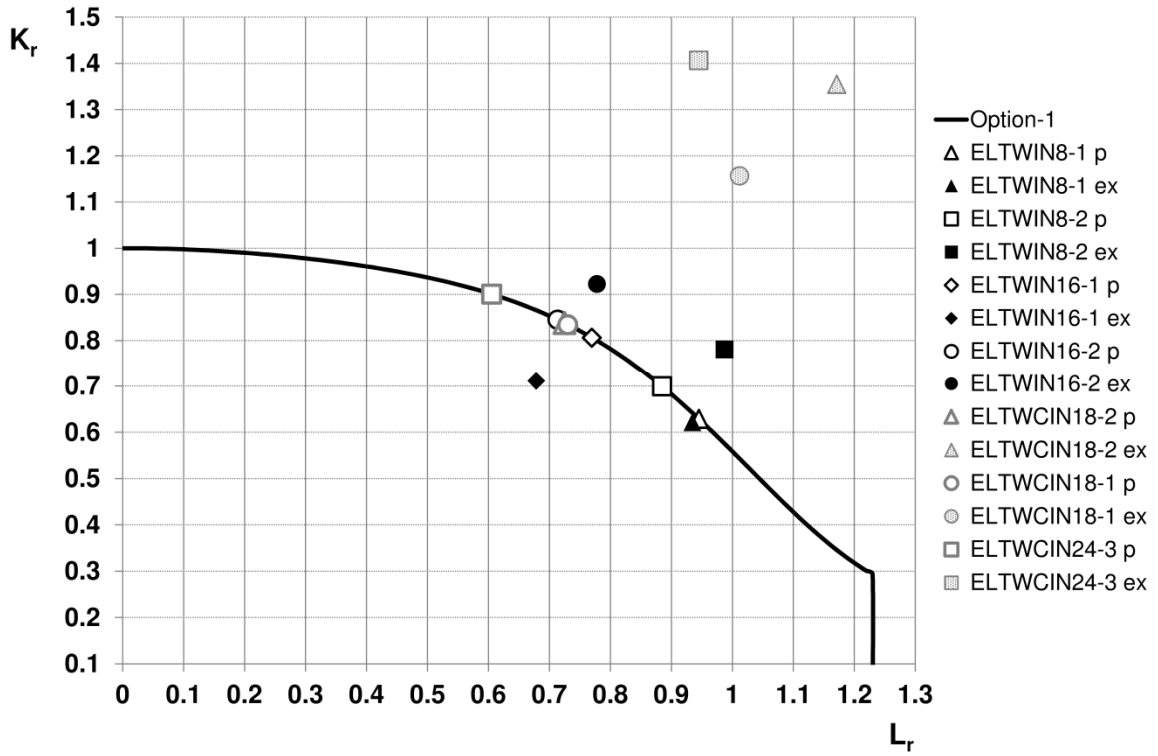| Test Number	Experimental Initiation Load $P_{0.2}^{ex}$, kN		Predicted Initiation Load $P_{0.2}^{p}$, kN		Difference, % $\dfrac{(P_{0.2}^{p} - P_{0.2}^{ex})}{P_{0.2}^{ex}}100$
	L_r	K_r	L_r	K_r	
ELTWIN8-1	113.0		114.3		1.1
	0.9344	0.6219	0.9451	0.6289	
ELTWIN8-2	89.7		80.4		-10.4
	0.9872	0.7808	0.8846	0.6995	
ELTWIN16-1	647.6		734.6		13.4
	0.6783	0.7110	0.7694	0.8065	
ELTWIN16-2	594.3		544.8		-8.3
	0.7781	0.9223	0.7133	0.8454	
ELTCWIN18-2	1117.6		691.6		-38.1
	1.1711	1.3546	0.7247	0.8381	
ELTCWIN18-1	668.0		482.2		-27.8
	1.0116	1.1565	0.7301	0.8345	
ELTCWIN24-3	1321.3		846.4		-35.9
	0.9448	1.4063	0.6052	0.9007	
ELTWEX8-4	125.0		140.4		12.3
	0.9184	0.4601	1.0316	0.5168	
ELTWEX16-3	1382.1		1209.3		-12.5
	1.0424	0.6864	0.9677	0.6005	
ELTWEX16-4	1004.2		927.8		-7.6
	0.8814	0.8326	0.8144	0.7692	
ELTWEX16-5	748.4		690.1		-7.8
	0.7642	0.9225	0.7047	0.8506	
ELTWCEX-C-24-2	1824.7		1106.2		-39.4
	1.1033	1.4367	0.6688	0.8709	
ELTWCEX-C-24-1	1411.2		767.4		-45.6
	1.0772	1.6705	0.5858	0.9084	

Fig. 8 Circumferentially through-wall cracked elbows under opening mode. Predicted and experimental initiation load points (Δa=0.2 mm) on FAD

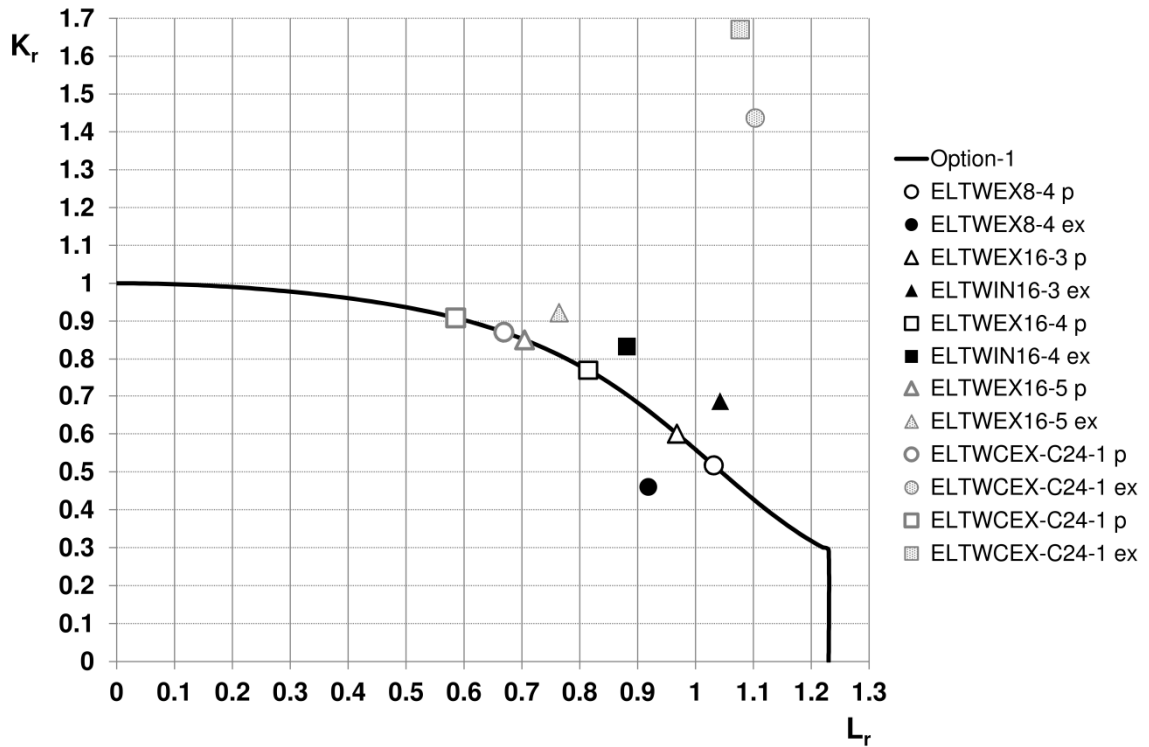**Fig. 9** Circumferentially through-wall cracked elbows under closing mode. Predicted and experimental initiation load points (Δa=0.2 mm) on FAD

5 Finite element analysis

Although the elbow solutions in Sections 3.1.2 and 3.2.2 have been obtained from modern finite element analyses, these analyses were for pure bending. In contrast, the loading in Figure 3 induces a combination of bending and tension or compression at the mid-section of the elbow, as a force is applied through the servo-hydraulic actuator. Therefore, finite element (FE) simulations have been performed to assess the influence of the loading on the stress distribution at the mid-section of a defect-free elbow. Elastic FE analyses were performed using the commercial software ABAQUS. Two different loading cases were simulated: moment created by rotation and moment created by a concentrated force. In both cases, the geometry of the ELTWEX8-4 elbow without a defect was subjected to the same magnitude of in-plane closing bending moment, but applied in two different ways.

In order to induce pure in-plane bending, rotation was applied to the ends of an elbow using the MPC (multi-point constraint) constraint type option within ABAQUS. The end surfaces of the elbow were constrained by one master node located in the middle of the cross section. Then rotation was applied to the master node. This constraint type allows rotation to be transferred from the master node via constrained slave surfaces to the elbow. The MPC option ensures that the rotated end surfaces remain straight during bending. In order to reproduce the test conditions of Figure 3c, a concentrated force and pin-type constraint were used. The concentrated force was applied to the master point at the end of the elbow. The pin type constraint was applied to the master node at the other end of the elbow.

The material was considered as isotropic elastic. The values of Young's modulus and Poisson's ratio were taken as 203 GPa and 0.3, respectively.

20-node quadratic brick elements with full integration (element type C3D20 within ABAQUS) were used for both cases. A full model of the elbow was used. Fig. 10 shows the FE mesh of a quarter of the elbow. The model has four element layers through the thickness.
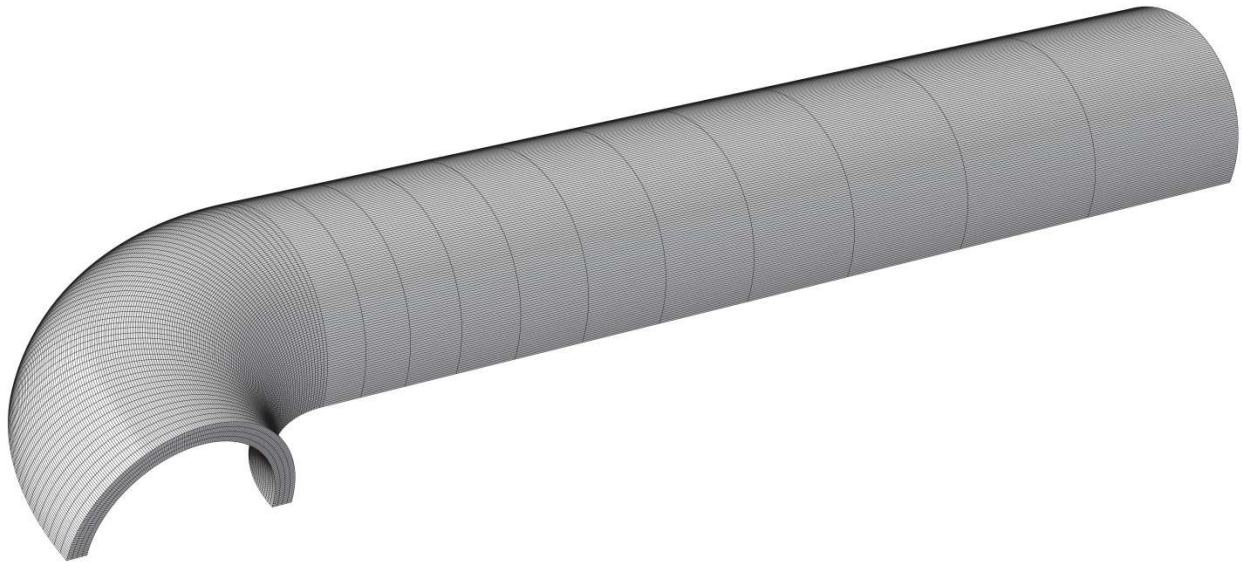

Fig. 10 The mesh of quarter model

In [13], mesh sensitivity analyses of an elbow subjected by in-plane bending moment have been reported. It was shown that the use of four layers of elements through the thickness is sufficient for elbow analysis. In the analyses reported here, the elbow cross-section was divided into 344 elements along the circumferential direction.

The stress distribution at the mid-section of the elbow is presented in Fig. 11 and Fig. 12. In these figures the start of each curve corresponds to the extrados point. The position at any point around the mid-section is described by the angle φ. The stress values were taken from each of 345 nodes along the external perimeter of the cross-section. Fig. 11 shows the axial and Fig. 12 the circumferential stress

distribution. The results show no significant difference in the stress distribution resulting from pure bending moment and that from a bending moment created by a concentrated force. Therefore, it is concluded that the closed form limit load and stress intensity factor solutions developed for pure bending (see sections 3.1.2, 3.2.2.1 and 3.2.2.2) are applicable to elbows loaded as shown in Fig. 3c.
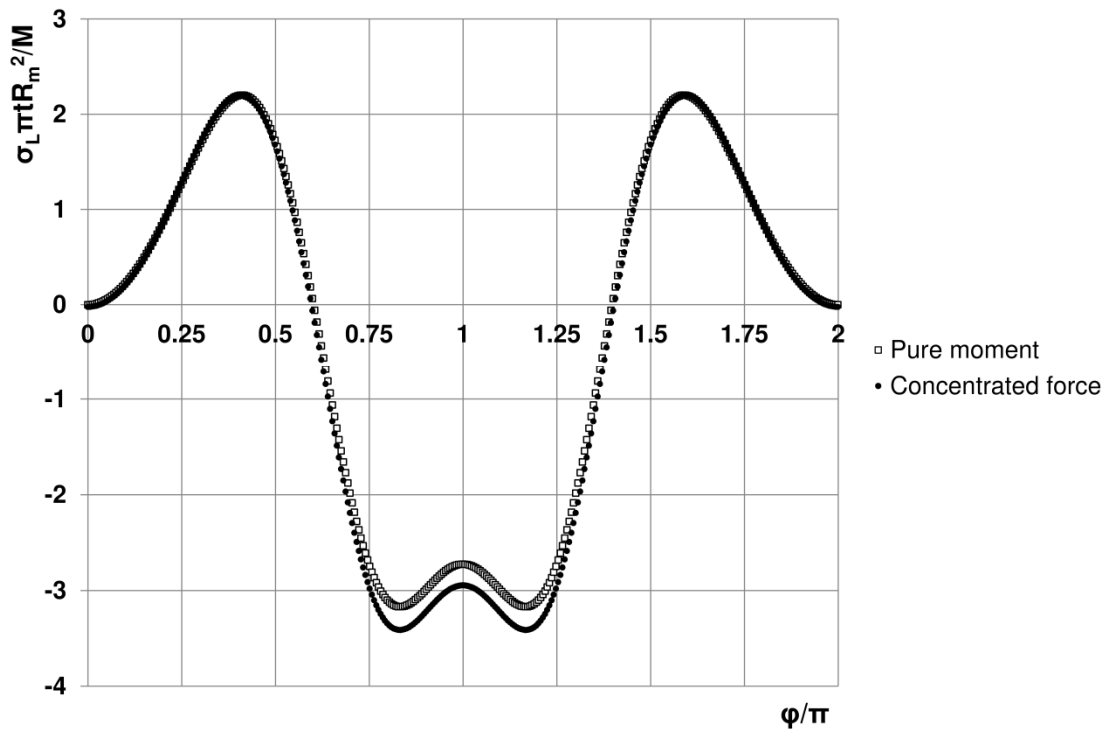
Fig. 11 Longitudinal stress distribution along external perimeter of elbow at mid-section
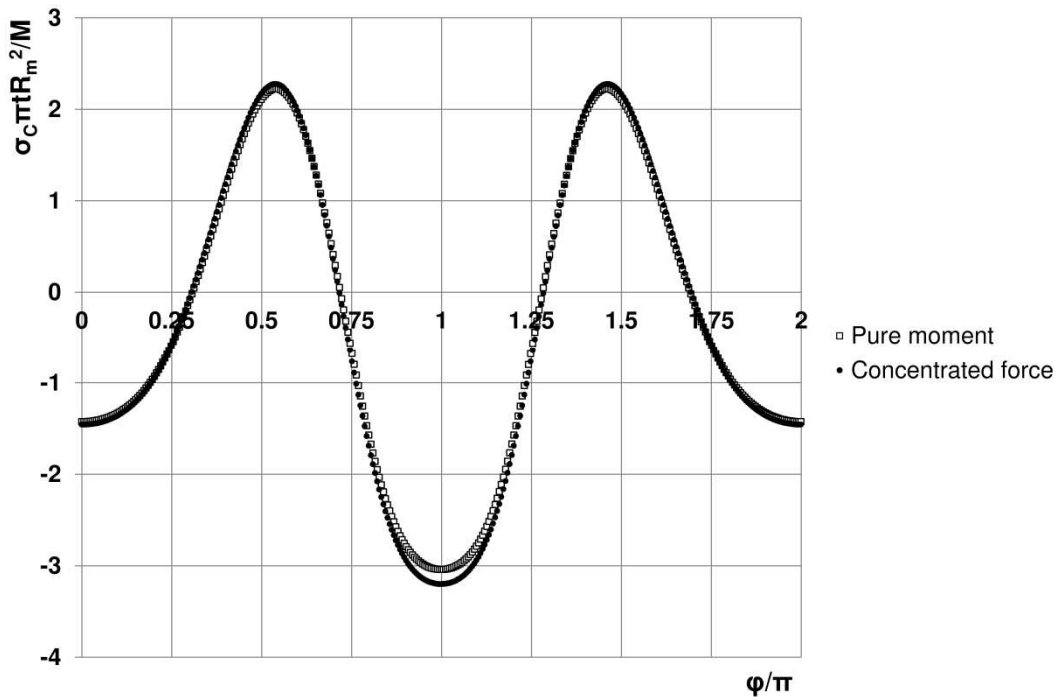

Fig. 12 Circumferential stress distribution along external perimeter of elbow at mid-section

Consider, first, the six through-wall cracked straight pipes under pure bending (tests denoted SPBMTWC). It can be seen from Table 7 and Figure 6 that the predicted loads for ductile initiation are generally close to the experimental values. On average, the predicted initiation loads are a little under 5% less than the experimental initiation loads, although for one test the under-prediction is about 15%. The predictions are highly accurate for the pipes with outer diameter D_o=406mm (tests denoted SPBMTWC16) and more conservative for the smaller diameter pipes (diameter D_o=219mm, tests denoted SPBMTWC8). There is no clear systematic effect of crack size. As R_m/t is similar for the two pipe diameters (see Table 2), the T-stress is predominantly a function of crack size (angle) and there is higher normalised constraint loss for smaller cracks (test SPBMTWC8-1 has the lowest value of θ/π, see Table 2). There is no systematic effect of constraint loss on the ductile initiation load, consistent with the work of Hancock et al. [30] and others.

A greater effect of constraint loss would, however, be expected on ductile tearing and maximum load assessments. Although ductile tearing data are not available for the material of the six through-wall cracked straight pipes under pure bending, such data have been inferred in Section 4.2 by assuming that the R6 Option 1 curve is accurate and the results are shown in Figure 7. It can be seen that there is a clear difference between the inferred tearing curves for the 209 mm diameter pipes and those for the 406mm diameter pipes. There are two possible reasons for this. The first is that the resistance curve simply reflects the different materials of the two pipe diameters. Although the tensile and initiation fracture toughness data in Table 1 show some differences, these are less than 10% whereas the J-resistance values in Figure 7 differ by about a factor of 2 at larger crack extensions. This suggests that there may be greater constraint loss in the smaller diameter pipes than in the larger diameter pipes, leading to the higher resistance curves. Although clear systematic trends are not shown by the T-stress solutions in Table 7 at the initiation loads, the absolute values for the 209mm diameter pipes are on average about 50% higher (i.e. T-stress values are more negative) than those for the 406mm diameter pipes. This suggests that there is an influence of constraint loss on the ductile crack growth observed in the pipes, although this is the subject of ongoing study.

Secondly, consider the two through-wall cracked straight pipes under combined pressure and bending (tests denoted PRSPTWC8). Here the predicted initiation loads are about 30% below the experimental values for both tests (see Table 7 and Figure 6). Indeed, ductile initiation in both tests occurs close to the plastic collapse load, as defined by the cut-off $L_r = L_r^{max}$. It can be seen from Table 7 that the constraint loss in these tests is not significantly different from the tests in pure bending and therefore the increased experimental initiation loads can not be explained in terms of constraint loss. However, the cracks in these two tests were not fatigue pre-cracked under bending, as in the other tests considered above, and this is the most likely explanation for the increased ductile initiation loads in these tests.

Next, consider the elbow tests with intrados cracks under opening mode bending (Table 8 and Figure 8, tests denoted ELTWIN). For the pipe diameters of 219mm and 406mm (denoted ELTWIN8 and ELTWIN16 directly comparable to the straight pipe tests), the experimental initiation loads are on average very close to the predicted initiation loads, although with increased scatter (about $\pm10\%$ between predicted and experimental values). For the elbows with larger pipe diameters of D_o =460mm, 610mm (denoted ELTWIN18 and ELTWIN24), the predicted initiation loads are significantly below the experimental initiation loads (by 28%-38%). However, the larger diameter elbows were not fatigue pre-cracked and had V-shape notches and, as noted in Section 2.1, there is some uncertainty about the fracture toughness for these larger diameter pipes and the values of initiation fracture toughness, $J_{0.2}$, can exceed the bold values in Table 1, used in the assessments, by 40%-60%. Had the higher values of initiation fracture toughness from Table 2 been used, then the values of K_r at the experimental initiation loads would have been reduced by 20%-30%. Although the

predicted initiation loads would still have exceeded the experimental initiation loads, the conservatism would have been comparable to that for the smaller diameter pipes.

Finally, consider the elbow tests with extrados cracks under closing mode bending (Table 8 and Figure 9, tests denoted ELTWEX). For these tests, the trends are very similar to those of the elbow tests under opening mode bending. For the smaller pipe diameters (denoted ELTWEX8 and ELTWEX16), the experimental initiation loads are on average very close to the predicted initiation loads but predictions for the larger diameter elbows (denoted ELTWCEXC-24) are conservative by about 40%.

As with the straight pipe tests under combined pressure and bending (PRSPTWC8), the larger diameter (D_0= 460mm and 610mm) elbows were not fatigue pre-cracked. Instead, they were tested with fabricated notches. The explanation for the experimentally high loads for ductile initiation relative to the prediction is therefore also likely to be due to the sharpness of the initial defect.

Recognising that there is some experimental uncertainty in detecting the initiation load in large-scale tests, it can be seen that where the fracture toughness is well known, the predicted initiation loads are on average close to the experimental initiation loads, with a tendency for some small conservatism and greater scatter in elbow tests than in straight pipes under bending. At ductile initiation, there does not appear to be any systematic effect of constraint loss, as might be evidenced by an effect of crack size for example. For larger diameter elbows there is some uncertainty about the appropriate value of fracture toughness and the use of a lower estimate leads to increased conservatism in assessments in these cases. It appears that there may be an influence of constraint loss on the ductile crack growth observed in the tests, although this is the subject of ongoing study.

7 Conclusions

This paper has presented assessments of the loads for ductile fracture initiation in 21 large-scale piping tests, consisting of 8 straight pipes and 13 elbows. It has been shown that the use of modern solutions for stress intensity factor and limit load, recently presented in the literature, in conjunction with standard failure assessment diagram methods, leads to generally accurate assessments of the loads for ductile crack initiation, with a tendency for some small conservatism and greater scatter in elbow tests than in straight pipes under bending. Some limited analysis, suggests that constraint loss is not a major contributor to the initiation fracture assessments but may have some influence on the ductile crack extension.

Acknowledgements

References

[1] R6: Assessment of the integrity of structures containing defects, Revision 4, including subsequent updates to Amendment 11, EDF Energy Generation, Gloucester, UK (2015).

[2] BS 7910:2013+A1:2015, Guide to methods for assessing the acceptability of flaws in metallic structures. British Standard Institution, London, UK; Incorporating Corrigenda 1 and 2, (2016).

[3] API 579-1/ ASME FFS-1, Fitness-for-service, American Petroleum Institute/ASME, Washington DC (2016).

[4] RSE-M Code, In-service Inspection Rules for the Mechanical Components of PWR Nuclear Islands, Appendix 5.4 – Analytical Methods for Calculating Stress Intensity Factors and J Integral, 2010 Edition, AFCEN, Paris (2010).

[5] X-K Zhu and B N Leis, Evaluation of burst pressure prediction models for line pipes, Int J Pres Ves Piping **89**, 85-97 (2012).

[6] B Bedairi, D Cronin, A Hosseini and A Plumtree, Failure prediction for crack-in-corrosion defects in natural gas transmission pipelines, Int J Pres Ves Piping **96-97**, 90-99 (2012).

[7] J Chattopadhyay, B K Dutta and H S Kushwaha, Experimental and analytical study of three point bend specimens and throughwall circumferentially cracked straight pipe, Int J Pres Ves Piping **77**, 455-471 (2000).

[8] J Chattopadhyay, T Pavan Kumar, B K Dutta and H S Kushwaha, Fracture experiments on through wall cracked elbows under in-plane bending moment: test results and theoretical/numerical analyses, Engng Fract Mech **72**, 1461-1497 (2005).

[9] J Chattopadhyay, B K Dutta and K K Vaze, Development of new correlations for improved integrity assessment of pipes and pipe bends, Nucl Engng Design **269**, 108-115 (2014).

[10] N-H Kim, C-S Oh, Y-J Kim, J-S Kim, D W Jerng and P J Budden, Limit loads and fracture mechanics parameters for thick-walled pipes, Int J Pres Ves Piping **88**, 403-414 (2011).

[11] Y Li, Y Lei and Z Gao, Global limit load solutions for thick-walled cylinders with circumferential cracks under combined internal pressure, axial force and bending moment – Part II: Finite element validation, Int J Pres Ves Piping **114**-**115**, 41-60 (2014).

[12] S-P Hong, J-H An, Y-J Kim, K Nikbin and P J Budden, Approximate elastic stress estimates for elbows under internal pressure, International Journal of Mechanical Sciences **53**, 526-535 (2011).

[13] J-H An, S-P Hong, Y-J Kim and P J Budden, Elastic stresses for 90° elbows under in-plane bending, International Journal of Mechanical Sciences **53**, 762-776 (2011).

[14] T C Micheal, AR Veerappan and S Shanmugam, Effect of internal pressure and shape imperfections on plastic loads op pipe bends under in-plane closing moment, Engineering Fracture Mechanics **105**, 1-15 (2013).

[15] T C Micheal, AR Veerappan and Shanmugam, Effect of ovality and variable wall thickness on collapse loads in pipe bends subjected to in-plane bending closing moment, Engineering Fracture Mechanics **79**, 138-148 (2012).

[16] A Buckshumiyan, A R Veerappan and S Shanmugam, Plastic collapse loads in shape-imperfect pipe bends under in-plane opening bending moment, Int J Pres Ves Piping **111-112**, 21-26 (2013).

[17] J W Kim, M S Yoon and C Y Park, The effect of load-controlled bending load on the failure pressure of wall-thinned pipe elbows, Nuclear Engineering and Design **265,** 174-183 (2013).

[18] C-G Kim, K-D Bae and Y-J Kim, Quantification of thickness effects for circumferential through-wall cracked pipe bend with un-uniform thickness under in-plane opening bending, Procedia Engng 130, 1779-1787 (2015).

[19] S Zhang, X Wang, B Song and D Zhao, Limit analysis based on GM criterion for defect-free pipe elbow under internal pressure, International Journal of Mechanical Sciences **78**, 91-96 (2014).

[20] J-J Han, K-H Lee, N-H Kim, Y-J Kim, D W Jerng and P J Budden, Comparison of existing plastic collapse load solutions with experimental data for 90° elbows, Int J Pres Ves Piping **89**, 19-27 (2012)

[21] J-H An, Y-J Kim and P Budden, Elastic stress intensity factors and crack opening displacements for circumferential through-walled cracked elbows, Engng Fract Mech **77**, 2821-2839 (2010).

[22] Y Lei, Review of Limit Loads Solutions for Defective Pipe Bends, Report E/REP/BBGB/0060/GEN/09 Revision 000, EDF Energy Nuclear Generation, Gloucester, UK (2011).

[23] Y-J Kim, Y-I Kim and T-K Song, Finite element plastic loads for circumferential cracked pipe bends under in-plane bending, Engng Fract Mech **74**, 643-668 (2007).

[24] Y Lei, Y Li and Z Gao, Global limit load solutions for thick-walled cylinders with circumferential cracks under combined internal pressure, axial force and bending moment, Part I: Theoretical solutions, Int J Pres Ves Piping **114-115**, 23-40 (2014).

[25] T Lewis and X Wang. The $T-$stress solutions for through-wall circumferential cracks in cylinders subjected to general loading conditions. Engng Fract Mech **75** 3206-3225 (2008).

[26] J Chattopadhyay, A K S Tomar, B K Dutta and H S Kushwaha, Closed form collapse moment equation of throughwall circumferentially cracked elbows subjected to in-plane bending moment, ASME J Pres Ves Technology **126**, 307-317 (2004).

[27] J Chattopadhyay and A K S Tomar, New plastic collapse moment equations of defect-free and throughwall circumferentially cracked elbows subjected to internal pressure and in-plane bending moment., Engng Fract Mech **73**, 829 – 854 (2006).

[28] A Zahoor, Closed form expressions for fracture mechanics analysis of cracked pipes, ASME J Pres Ves Technology **107**, 203-205 (1985).

[29] J Chattopadhyay, H S Kushwaha and E Roos, Some recent developments on integrity assessment of pipes and elbows, Part I: Theoretical investigations. Int J Solids Structures 43, 2904-2931 (2006).

[30] J W Hancock, W G Reuter and D M Parks, Constraint and toughness parameterized by T, in Constraint Effects in Fracture (edited by E M Hackett, K-H Schwalbe and R H Dodds), ASTM STP 1171, 21-40 (1993).

HIGHLIGHTS

- This paper presents assessments of the loads for ductile fracture initiation in 21 large-scale piping tests, consisting of 8 straight pipes and 13 elbows.
- It has been shown that the use of modern solutions for stress intensity factor and limit load, recently presented in the literature, in conjunction with standard failure assessment diagram methods, leads to generally accurate assessments of the loads for ductile crack initiation.
- The effects of constraint are found not to be a major contributor to the initiation fracture assessments.